Changes in Crack Shape and Saturation in Laboratory-Induced Seismicity by Water Infiltration in the Transversely Isotropic Case with Vertical Cracks

Koji Masuda

Geological Survey of Japan, National Institute of Advanced Industrial Science and Technology, Tsukuba 305-8567, Japan

Short title: Changes in Crack Shape and Saturation in Laboratory-Induced Seismicity

Corresponding author: Koji Masuda

koji.masuda@aist.go.jp, phone 81-029-861-3994

Summary

Open cracks and cavities play important roles in fluid transport. Underground water penetration induces microcrack activity, which can lead to rock failure and earthquake. Fluids in cracks can affect earthquake generation mechanisms through physical and physicochemical effects. Methods for characterizing the crack shape and water saturation of underground rock are needed for many scientific and industrial applications. The ability to estimate the status of cracks by using readily observable data such as elastic-wave velocities would be beneficial. We have demonstrated a laboratory method for estimating the crack status inside a cylindrical rock sample based on a vertically cracked transversely isotropic solid model by using measured P- and S-wave velocities and porosity derived from strain data. During injection of water to induce failure of a stressed rock sample, the crack aspect ratio changed from 1/400 to 1/160 and the degree of water saturation increased from 0 to 0.6. This laboratory-derived method can be applied to well-planned observations in field experiments. The in situ monitoring of cracks in rock is useful for industrial and scientific applications such as the sequestration of carbon dioxide and other waste, induced seismicity, and measuring the regional stress field.

Key words

Fracture and flow; Geomechanics; Hydrogeophysics; Acoustic properties; Induced seismicity

1. Introduction

Pore pressure change and fluid migration are known to cause rock deformation and failure (e.g., Healy et al., 1968; Lei et al., 2008; Ohtake, 1987; Prioul et al., 2000; Raleigh et al., 1976). Because open cracks and cavities play important roles in fluid transport (Caine et al., 1996; Rutqvist et al., 2008), the evolution of microcracking in the presence of underground fluids and crustal stresses is a critical factor in geothermal energy extraction (e.g., Fehler, 1989), carbon dioxide capture and storage (e.g., Baines & Worden, 2004; Hangx et al., 2010), waste disposal, and induced seismicity (Ellsworth et al., 2013; Schultz et al., 2020). Methods to measure the volume and shape of cavities and cracks would be of great assistance in planning industrial and scientific applications, including characterization of regional stress fields and sequestration of carbon dioxide and other waste. Methods are particularly needed for in situ monitoring microcrack evolution at depths of around 1 km.

In this research on microcrack activity caused by hydrological effects inside rock samples, we conducted laboratory studies with the aim of constructing a basic model for these underground processes. This paper describes an in situ monitoring method for estimating the crack shape and degree of water saturation in rock samples from measured P- and S-wave velocities and porosity changes.

Field experiments on water-induced seismicity have been conducted for scientific and industrial purposes. Experiments conducted in Matsushiro, Japan (Ohtake, 1987), and Rangely, Colorado, USA (Raleigh et al., 1976), have revealed relationships between water injection and induced microearthquakes. Water-injection experiments conducted in deep boreholes, such as the

German Continental Deep Drilling Program (KTB), have revealed characteristics of induced seismicity (Jost et al., 1998; Zoback & Harjes, 1997). Other studies have examined microearthquakes induced by water injection to infer seismic mechanisms and movements of fluids (e.g., Eyre et al., 2019, 2020; Lei et al., 2008; Prioul et al., 2000; Schultz et al., 2017, 2018; Wang et al., 2020). Such studies yield information on the relationship between water injection and initiation of microcracking; however, it is hard to obtain sufficient information about crack shape and degree of water saturation for modeling underground crack and fracture systems. Because of the difficulty of determining crustal stresses underground and distributing observation stations optimally, it is difficult to construct basic models using field studies.

To investigate the shape of microcracks induced in rock samples, we studied hydromechanical effects on the complex processes that control rock failure in the laboratory. Laboratory studies enable us to tightly control conditions and precisely measure data such as sample deformation and velocity changes in P and S waves. Laboratory studies are useful for constructing physical models for basic mechanisms that take place in long-term geological processes (Benson et al., 2008; Burlini et al., 2009; Masuda, 2013; Masuda et al., 2012). For example, Kranz et al. (1990), Lockner and Byerlee (1977), Masuda et al. (1990), Lockner et al. (1991), and Scholz (1968) investigated microfracturing through acoustic emission (AE) inside rock samples and developed techniques for analyzing AE. The relationship between water migration and induced microfractures also has been investigated in the laboratory (e.g., Masuda et al., 1990, 1993; Stanchits et al., 2011).

In this study, we developed a procedure for estimating crack status inside a rock sample based on a vertically cracked transversely isotropic solid model. We estimated two crack characteristics, crack shape and the degree of water saturation, and their changes during water migration into a granitic rock subjected to confining pressure and differential stress.

2. Sample and Methods

A cylinder (50 mm in diameter and 100 mm in length) of medium-grained Inada granite with an average grain size of 5 to 6 mm was used for the experiment. A differential stress of 370 MPa, which corresponds to about 70% of fracture strength, was applied to the rock sample in the axial direction at a constant rate of 0.06 MPa/s under 30 MPa confining pressure and was held constant throughout the experiment. When the primary creep stage and AE caused by the initial loading had ceased, we injected distilled water into the bottom end of the sample at a constant pressure of 25 MPa until macroscopic fracture occurred. Figure 1 shows the stress conditions and the number of AE events as a function of time.

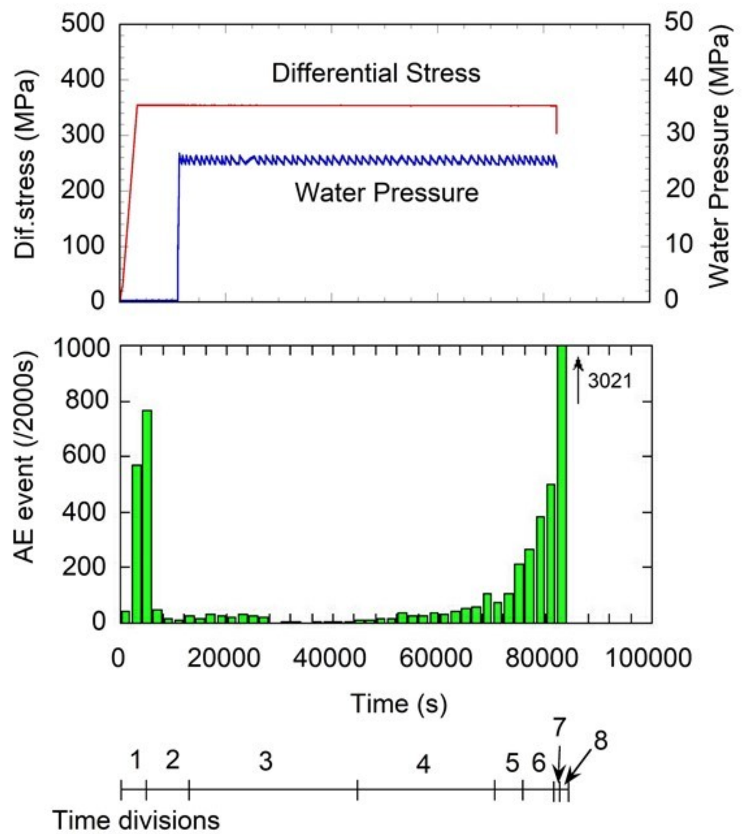

Figure 1

Figure 1. Changes in differential stress, water pressure at the injection site, and number of acoustic emission (AE) events as a function of time. Confining pressure was 30 MPa. Numbers at the bottom of the figure show time divisions for the plot of AE locations in Figure 8.

During water migration, P- and S-wave velocities, which propagated along five paths parallel to the top and bottom surfaces of the sample, were measured. Strains of the sample surface and AE were monitored and recorded. The locations of instrumentation on the surface of the rock sample are shown in Figure 2. Axial and circumferential strains were measured using six pairs of strain gauges at the midpoint of the sample's length as indicated by the large blue circles in Figure 2.

Piezoelectric transducers (PZTs) with 2-MHz resonant frequency were attached at the 18 places indicated by the small red circles in Figure 2 and inside the top and the bottom end-pieces. At 10 of these locations (1–5 and 10–14 in Figure 2), we attached transducers for P waves, vertical S waves (S_V), and horizontal S waves (S_H), in which the subscript specifies the direction of vibration. With the pulse transmission method, P-wave and horizontal and vertical S-wave velocities across the rock sample at five locations were measured (Figure 3). Because low-porosity aggregate was considered, the effect of porosity on the density of the sample could be ignored in calculating velocities (Anderson et al., 1974). In this study, the sample rock material was considered to be homogeneous because the wavelength of the wave velocity was longer than the scale length of heterogeneity in the rock. The sampling rate of the digital recording system was 50 ns. AE signals were also recorded with all 18 P-wave transducers shown in Figure 2, plus the two transducers on the top and bottom of the rock sample. AE hypocenters were determined by the automatic arrival time and hypocenter determination method of Lei et al. (2004).

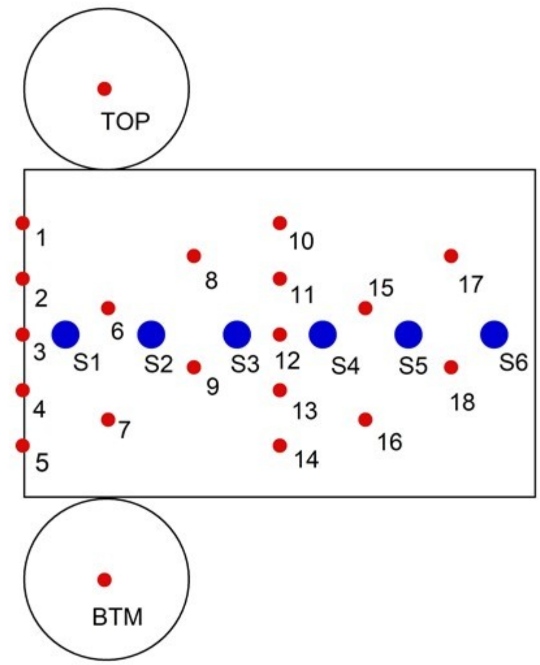

Figure 2

Figure 2. Locations of piezoelectric transducers and strain gauges on a rock sample. Schematic map of the cylindrical surface of the sample. Large blue circles (S1 to S6) indicate the locations of pairs of cross-strain gauges that monitored surface strains. Small red circles (1 to 18, TOP, BTM) indicate the locations of piezoelectric transducers.

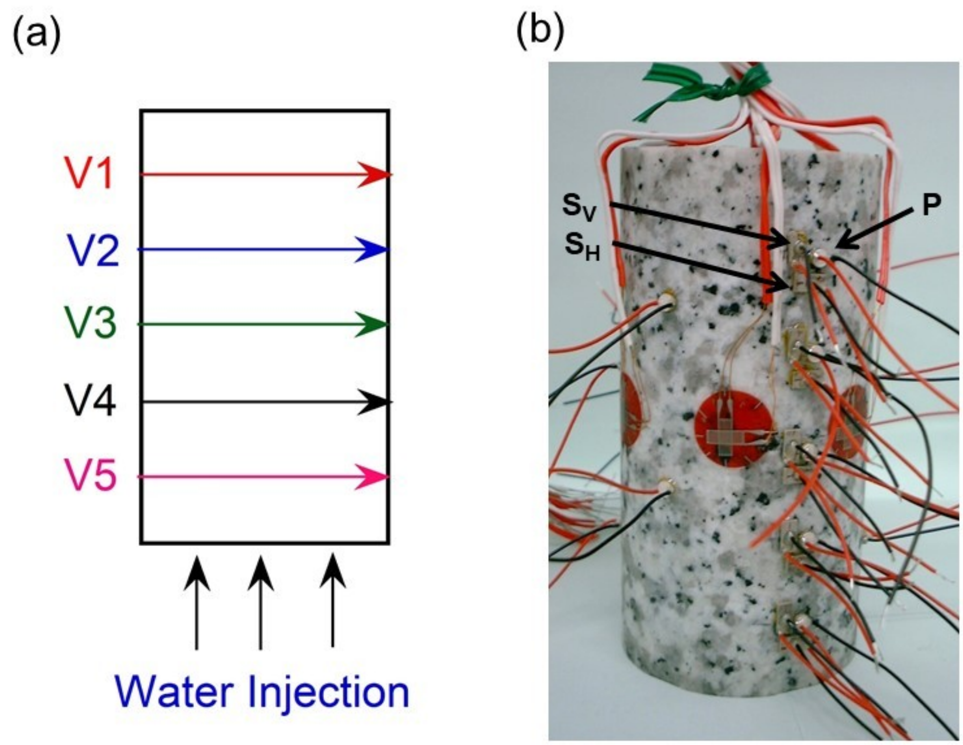

Figure 3

Figure 3. Paths of velocity measurements across the rock sample. (a) For P- and S-wave velocity measurements, elastic pulses were initiated from transducers V1 through V5 (at locations 1 through 5 in Figure 2) and received by transducers on the other side (at locations 10 through 14 in Figure 2). Water was injected uniformly from the bottom surface of the rock sample. (b) Photograph of the instrumented rock sample showing placement of transducers for detection of three types of elastic waves (locations 1–5 and 10–14 in Figure 2).

After the experiment, X-ray computer tomography (CT) images of the rock sample were created. Images were made in the plane perpendicular to the sample axis at 1-mm intervals, then combined into a three-dimensional model displaying the internal structure of the sample, including the shapes and locations of the fracture planes.

3. Results

3.1. P-wave velocity

The measured P-wave velocities in the rock sample are shown in Figure 4 as a function of time. During the initial loading stage, the P-wave velocity decreased due to the opening of new microcracks. After water injection began, the P-wave velocity increased on each measurement path in sequence from 5 to 1 as the water reached it (Figure 4) because open pores were partially filled with water, a phenomenon well documented in the literature (e.g., Budiansky & O'Connell, 1976; O'Connell & Budiansky, 1974). The P-wave velocity then gradually decreased due to undersaturation as the rate of cracking exceeded the rate of fluid flow, similar to the pattern documented by Masuda et al. (1990, 1993).

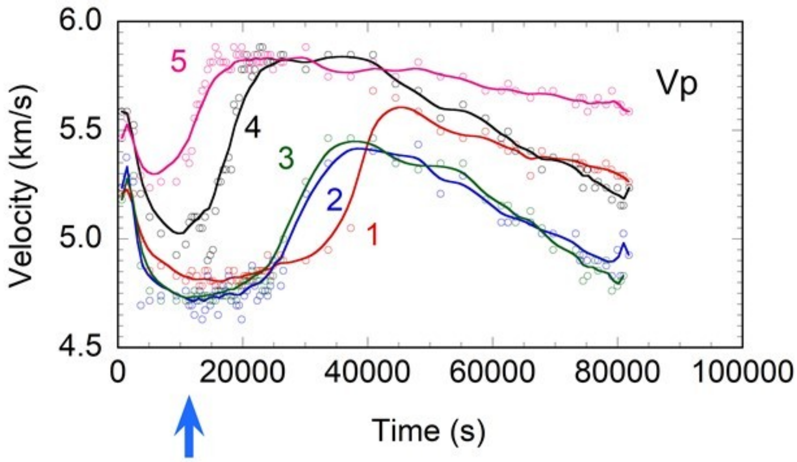

Figure 4

Figure 4. P-wave velocity for five transects of the rock sample (locations shown in Figure 3a) as a function of time. The blue arrow indicates the time when water injection started (modified from Masuda et al., 2013).

3.2. S-wave velocity

The velocities of the vertical and horizontal S waves are shown in Figure 5. Some transducers failed and yielded no data for the vertical S waves in measurement path 4 and for the horizontal S waves in paths 1, 3, and 4. At the times when the injected water front reached the measurement paths, as estimated from the P-wave velocity changes, the S-wave velocities increased slightly and then decreased gradually.

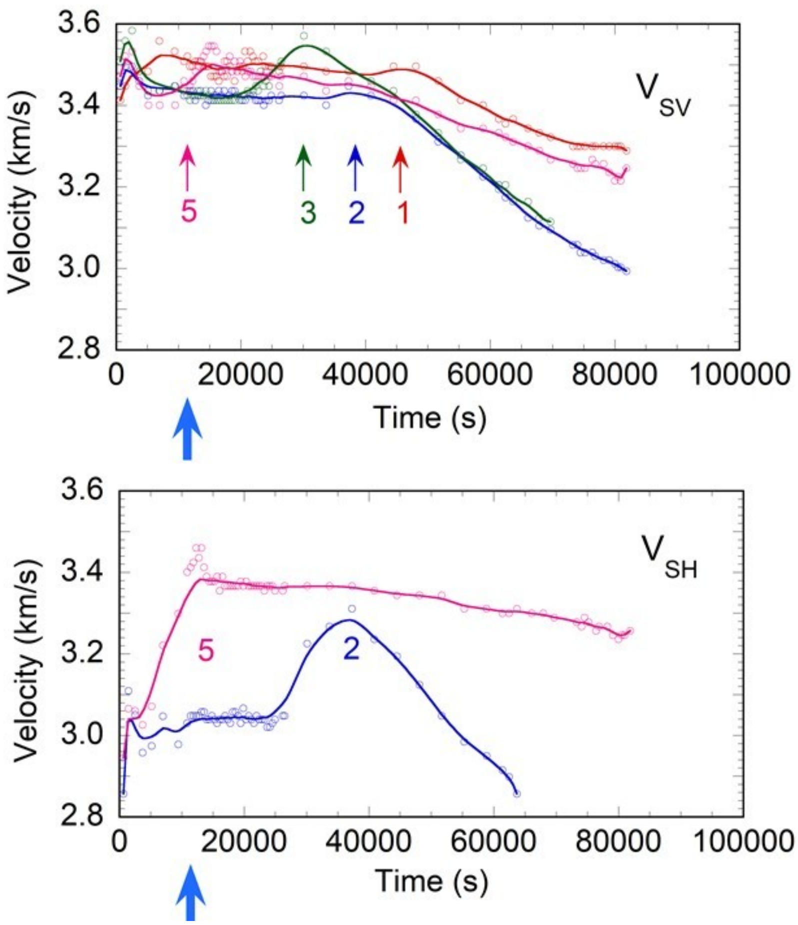

Figure 5

Figure 5. S-wave velocity with (a) vertical vibration S_V and (b) horizontal vibration S_H for four transects of the rock sample (locations shown in Figure 3a) as a function of time. The blue arrow indicates the time when water injection started. The numbered arrows show the estimated time when the water front reached the corresponding measurement path. Velocity data for several transects were not available.

The changes in Vp/Vs (where Vp and Vs are the P- and S-wave velocities, respectively) for vertical and horizontal S waves are plotted in Figure 6. This ratio tends to be somewhat higher in the absence of cracks, and saturating the cracks leads to an increase in Vp/Vs as described by Paterson and Wong (2005).

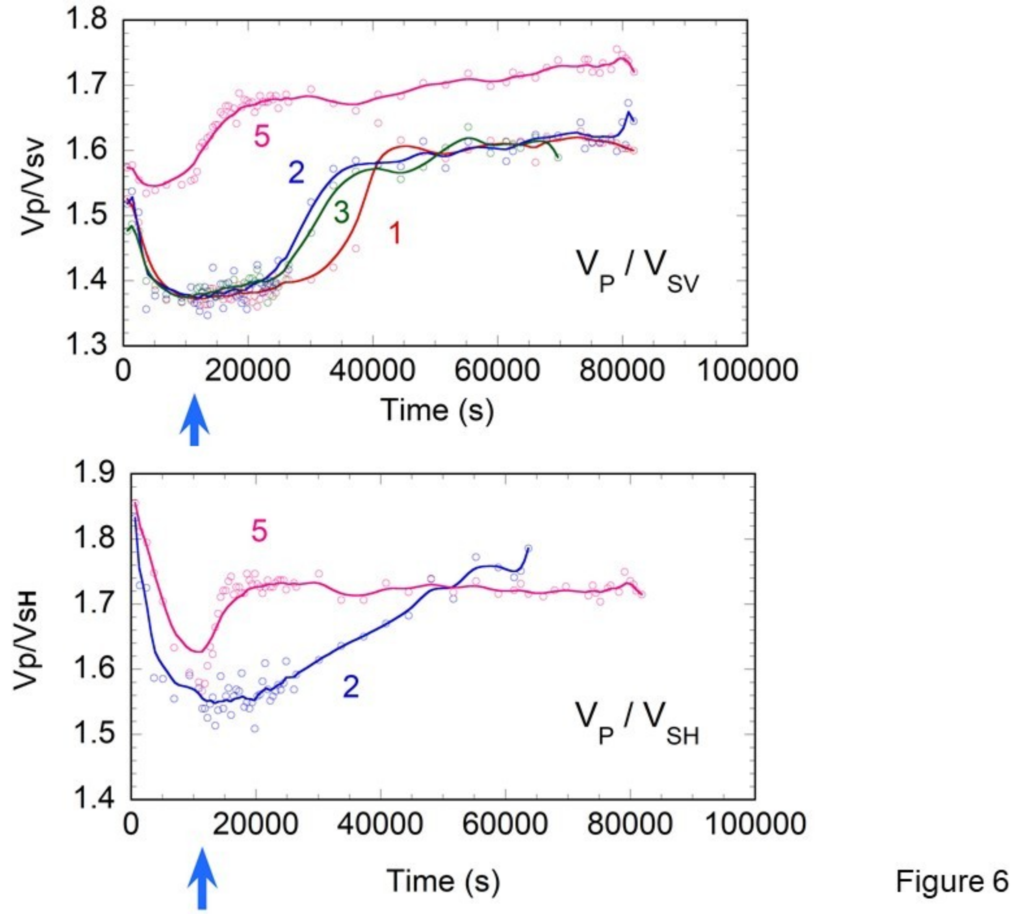

Figure 6. Vp/Vs ratios for S_V and S_H waves for transects of the rock sample (locations shown in Figure 3a) as a function of time.

3.3 Strain

The average axial, circumferential, and volumetric strains measured at the midpoint of the sample are shown in Figure 7. The strain gauges for axial strain at point S4 (Figure 2) failed, so no data were available. The plotted axial strain data were averaged over the remaining five locations. The circumferential strain shown is the average data for all six locations of the strain gauges. The volumetric strain was calculated as the axial strain plus two times the circumferential strain. After a time duration of 60,000 s, the circumferential strains measured at locations S3 and S4 rapidly increased and the strain gauges at these locations failed.

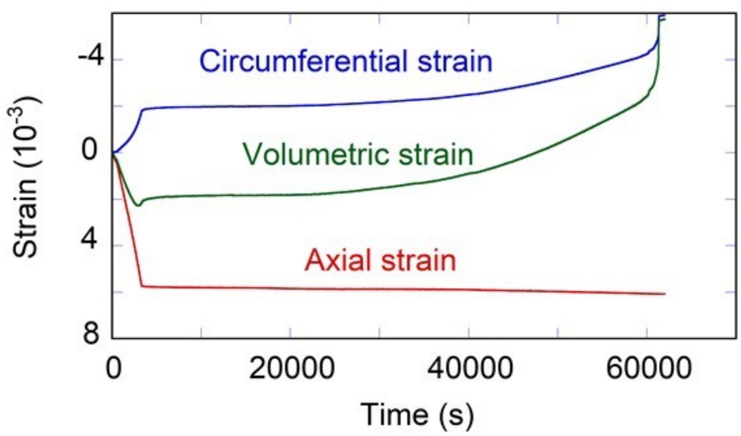

Figure 7

Figure 7. The average axial, circumferential, and volumetoric strains as a function of experimental duration.

3.4. AE hypocenter distribution

AE hypocenters were calculated by automated detection of P-wave arrivals. Figure 8 shows stereographic projections of AE hypocenter distributions for the eight time periods shown in Figure 1. The estimated location error for most AE events was less than 2 mm (e.g., Lei et al., 2004; Schubnel et al., 2003). Clustering of AE events was not observed except just before the final fracture (periods 7 and 8). In the initial loading stage (period 1), AE was distributed evenly throughout the sample, suggesting that the loading was achieved uniformly. Before the start of water injection (period 2) and just afterward (period 3), AE activity decreased. In periods 3 and 4, AE persisted in the middle of the sample and expanded upward, and in periods 5 and 6 AE activity increased. Just before the fracture (periods 7 and 8), AE clustered in the lower part at a location corresponding to the final fracture surface.

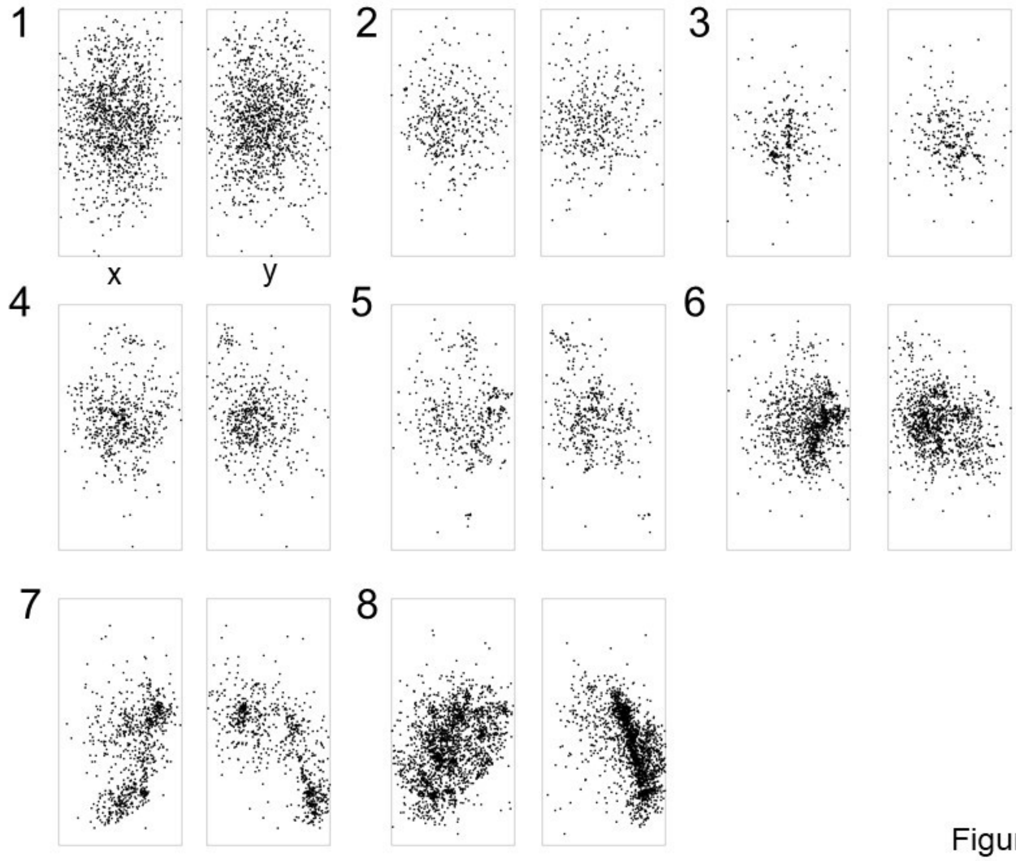

Figure 8

Figure 8. The vertical cross sections of the rock sample showing AE event locations during the eight time periods indicated in Figure 1.

3.5. X-ray CT imagery

After the experiment, we compiled 2D X-ray CT-images perpendicular to the sample axis, each representing 1 mm in thickness, at 1-mm intervals along the sample axis (99 total). The 3D image shown in Figure 9 was constructed from these 2D images. Figure 10 shows vertical cross sections derived from the 3D image. Three fracture surfaces (F1, F2, and F3) were recognized. The location and shape of surface F1 correspond to the fracture surface indicated by the AE hypocenter distributions (Figure 8). Fracture surface F2 formed at the edge of the sample, parallel to the sample surface. Fracture surface F3 was a small planar feature derived from the main rupture surface F1. The AE hypocenter distributions shown in Figure 8 indicate that rupture surface F1 formed and grew throughout the experiment whereas surfaces F2 and F3 formed just before the final fracture. According to microstructural studies by Moore and Lockner (1995), Paterson and Wong (2005), and Wong (1982), as the onset of marked localization of microcracking is approached, microcracks continue to be predominantly of axial orientation, but an increasing proportion are of inclined orientation or shear character.

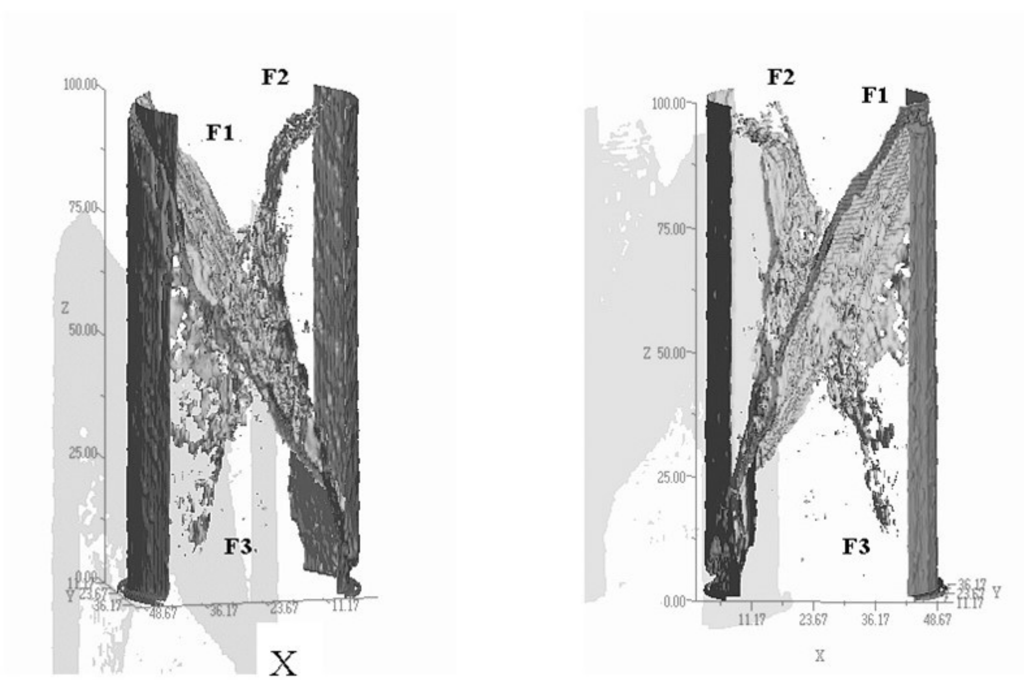

Figure 9

Figure 9. 3D CT image of the fracture planes (F1 through F3) of the sample from two viewpoints. The X-direction indicated in the left-hand image is the same as shown in Figure 10.

The right-hand image is shown from the opposite side of the left-hand image. The offset gray shadowy images are visual aids.

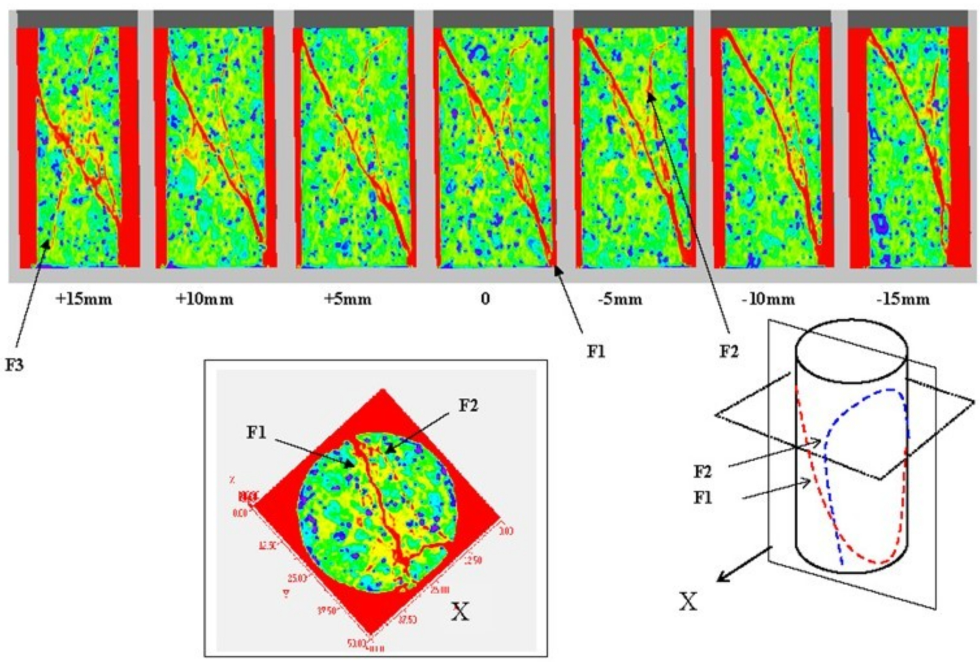

Figure 10

Figure 10. Horizontal CT cross section of the sample (65 mm from the sample base) after the experiment and vertical 2D images derived from 3D CT model at intervals of 5 mm from the center of the sample. Red color indicates low density. Progression from red to yellow, green, and blue colors indicates increasing density. The X-direction indicated in the left-hand image is the same as shown in Figure 9.

4. Discussion

4.1 Cracked solid model

We estimated crack parameters such as aspect ratio, the degree of water saturation, and their changes as a function of time. In the evaluation of these parameters, a cracked solid model (e.g., Crampin, 1978, 1984; Hudson, 1981; Nishizawa & Masuda, 1991; Soga et al., 1978) that approximates the rock as an elastic solid containing cavities representing pore space was applied. Because cavities are more compliant than solid material, they have the effect of reducing the elastic stiffness of the rock (e.g., Avseth et al., 2005; Mavko et al., 2009; Meglis et al., 1996).

In this study, we assumed a transversely isotropic medium in which vertical cracks of ellipsoidal, penny-shaped geometry distributed with the orientations of the crack normals randomly distributed in the plane perpendicular to the maximum stress as described in the Supporting Information (Figures S1 and S2) (e.g., Fossen, 2010; Scholz, 2002). Transverse isotropy is considered to be realistic when we consider seismic wave propagation in the Earth's crust. If this is the case, the velocities of S waves that propagate horizontally would be affected differently, as is seen in Figure 11; this effect is referred to as shear wave splitting (e.g., Anderson et al., 1974; Paterson & Wong, 2005). Figure 11 shows that the velocities of S waves with horizontal vibration are reduced more than those with vertical vibration for the data measured on both paths 2 and 5. The differences between Vs_V and Vs_H are larger for the data measured on path 2. This is because path 2 is near the center of the sample, whereas path 5 is close to the end of the sample where the crack volume is smaller than it is in the center. All of these observations support the use of a vertically cracked transversely isotropic modelin this study.

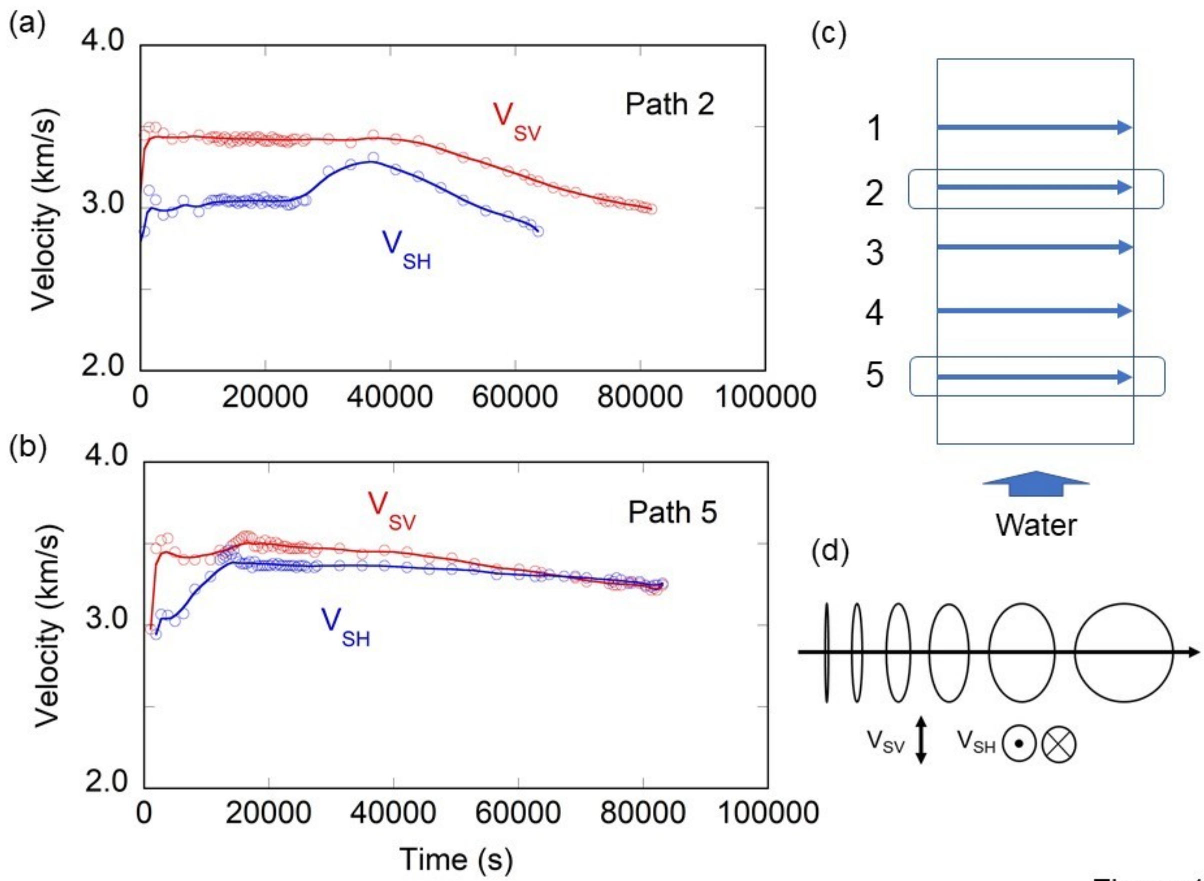

Figure 11

Figure 11. S-wave velocity with vertical vibration S_V and horizontal vibration S_H for (a) path 2 and (b) path 5. (c) Paths of the velocity measurements. (d) The wave propagation direction (thick blue arrow) and side view of the crack distribution in the transversely isotropic model with vertical cracks. The directions of vibration of the S_V and S_H waves are shown. Shear wave splitting was observed, supporting the assumption of transversely isotropic symmetry with vertical crack distribution.

The change in elastic wave velocities during the experiment was attributed to open cracks in the rock sample. The effect of cracks on the elastic properties of solids depends on various factors such as the shape, number, and orientation of the cracks. When very thin spheroidal cracks are randomly distributed in a solid, O'Connell and Budiansky (1974) showed that the effect of cracks on velocity is well described by the crack density parameter,

$$\varepsilon = N < a^3 > = \frac{3}{4\pi}\frac{\varphi}{\alpha} \quad , \qquad (1)$$

where <*a*> is the mean major axis of the crack ellipsoid; *N* is the number of cracks per unit volume of the solid; ϕ is the volume of cracks per unit volume of the solid, which can be written as

$$\varphi = \frac{4}{3}\pi < a^2 c > N \quad ; \qquad (2)$$

and α is the aspect ratio of a very thin spheroidal crack ($a = b >> c$), $\alpha = c/a$. According to Hudson (1981) and Soga et al. (1978), the effect of cracks on velocity, in terms of the ratio of velocities with and without cracks, is proportional to the crack density parameter ε at small values of ε,

$$(V/V_0)^2 = 1 - p_i\, \varepsilon, \qquad (3)$$

where V_0 and V are the elastic wave velocities of the rocks without and with cracks, respectively. The constants p_i can be calculated for P waves and two kinds of S waves under dry and saturated states (Table 1). Details regarding how to calculate the coefficients listed in Table 1 are described in the Supporting Information.

Table 1. The right sides of equation (3) with the constants p_i for dry and wet states. Details regarding the determination of the constants p_i are described in the Supporting Informantion.

	V_p	V_{SV}	V_{SH}
Dry	$1-\frac{71}{21}\varepsilon$	$1-\frac{8}{7}\varepsilon$	$1-\frac{15}{7}\varepsilon$
Wet	$1-\frac{8}{21}\varepsilon$	$1-\frac{8}{7}\varepsilon$	$1-\frac{8}{7}\varepsilon$

In partially saturated cases, P- and S-wave velocities can be interpolated from the dry and wet (saturated) velocities by using the degree of water saturation parameter ξ, which ranges from 0 (dry) to 1.0 (saturated). In this study, it is assumed that elastic constants in the partially saturated state can be expressed as the weighted average of the elastic constants of dry and saturated states (Voigt's average). Then the velocity V of a partially saturated state can be written as

$$V^2 = \xi V_w^2 + (1-\xi)\, V_d^2, \qquad (4)$$

where V_w and V_d are the velocities for the totally saturated and totally dry cases, respectively. From equations (1) through (4), equation (3) can be rewritten as

$$1-\left(\frac{V_{p,s}}{V_0}\right)^2 = p_i \frac{3}{4\pi}\frac{\varphi}{\alpha} . \qquad (5)$$

Here Vp and Vs are the P- and S-wave velocities for rocks that include cracks. The total crack volume ratio ϕ is calculated by using the measured surface strains of the rock sample as shown in the following section. Thus, given a set of α and ξ values, we can calculate curves of $1 - (V/V_0)^2$ versus ϕ for P and S waves. By comparing the calculated curves to the measured data shown in Figure 12, we estimate α and ξ and their variation with time by fitting for each measured experimental data set.

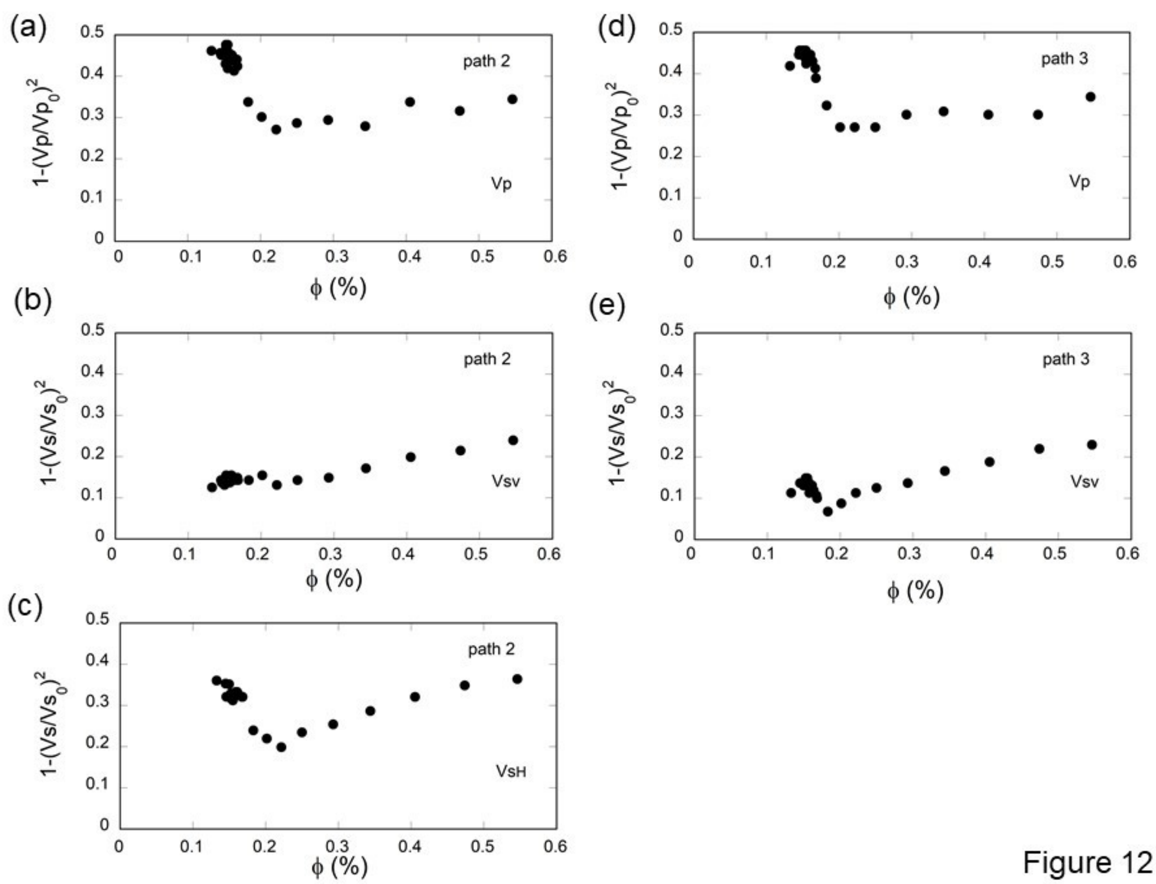

Figure 12. Measured data plotted for ϕ vs. $1 - (V/V_0)^2$. (a) Vp, (b) Vs_V, (c) Vs_H for path 2, and (d) Vp, (e) Vs_V for path 3.

4.2. Change in crack shape and degree of water saturation

Figure 13 shows the P-wave velocity change $1 - (Vp/Vp_0)^2$ as a function of ϕ, the volume of cracks per unit volume of the solid. We calculated ϕ based on strain data measured at the center of the rock sample (Figures 2 and 7). We first calculated the volumetric strain ε_v from the averages of the axial strain ε_Z and circumferential strain ε_θ as $\varepsilon_v = \varepsilon_Z + 2\varepsilon_\theta$. The stress–strain curve was linear in the early stage of loading except for the initial stage. Taking the linear part of the volumetric strain to represent the elastic volumetric strain, we fitted the ε_v versus stress line in the range from 1/9 to 1/3 of the failure stress by a straight line using the least-squares method. This stress range was used to avoid the effects of initial cracks at low stress levels and new cracks at high stress levels. We then calculated the dilatant strain ε_{dv} from the observed volumetric strain by subtracting the elastic volumetric strain predicted by the straight line (e.g., Brace et al., 1966; Paterson & Wong, 2005). We then used the calculated dilatant strain to represent ϕ. Here we used the P- and S-wave velocity data measured along paths V2 and V3 at the midpoint of the sample (Figure 3). Figure 13 shows that the curve of $\alpha = 1/400$ and $\xi = 0$ is best fitted to the data indicated by the arrow. Thus we estimated that the aspect ratio of the cracks before water injection (in the dry state, $\xi = 0$) was 1/400.

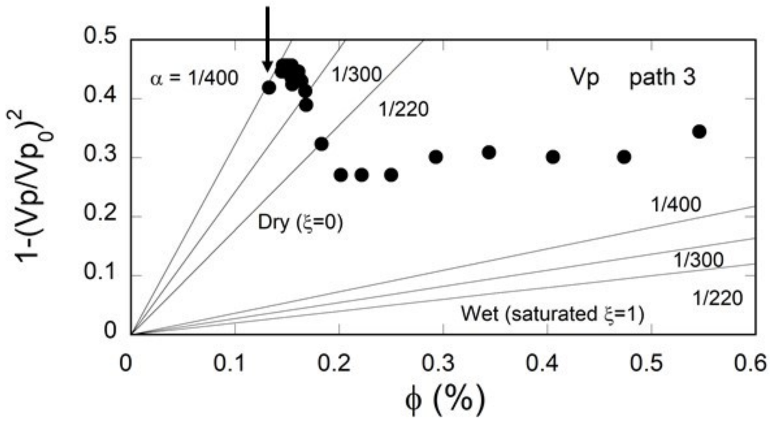

Figure 13

Figure 13. Procedure for estimating the pair of values for the crack aspect ratio and water saturation (α, ξ) for the case of ξ = 0. Values of $1 - (Vp/Vp_0)^2$ as a function of crack volume ϕ are plotted for Vp measured on path 3. Curves are shown for three values of α and endpoint values (0 and 1) of ξ. The data point indicated by the arrow, which was measured at the beginning of the velocity measurement, is nearly on the curve for the (α, ξ) pair (1/400, 0). Curves for the saturated case (ξ = 1) are shown as references.

To estimate α and ξ simultaneously after water injection for the case of ξ > 0, we need more than two kinds of data, such as Vp, Vs_V, or Vs_H. The best fitted set of (α, ξ) to the measured data was estimated by the grid search method using equations (4) and (5) with the constants p_i listed in Table 1. For example, Figure 14 shows the curves of α = 1/160 with ξ = 0, 0.2, 0.4, 0.6, 0.8, and 1.0 for Vp and ξ = 0.6 with α = 1/200, 1/180, 1/160, 1/140, 1/120, and 1/100 for Vs_V for path 3. For the last data point plotted, around $\phi = 0.55$, our best fitted set of (α, ξ) was α = 1/160 and ξ = 0.6.

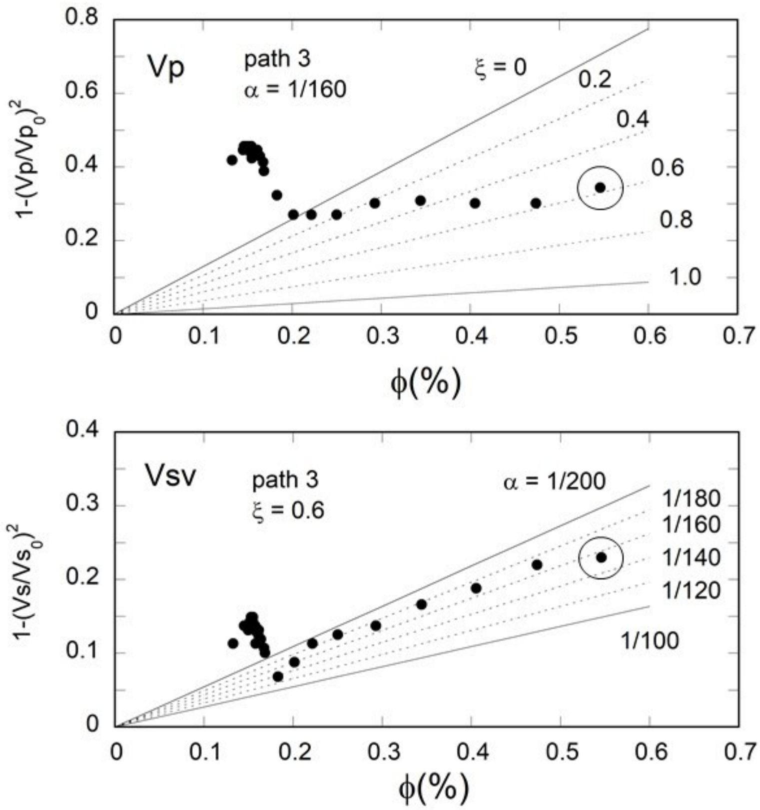

Figure 14

Figure 14. $1-(V/V_0)^2$ as a function of ϕ for Vp with curves for α = 1/160 and six values of ξ, and for Vs_V with curves for ξ = 0.6 and six values of α. Vp and Vs_V data were used to simultaneously estimate a pair of values for the crack aspect ratio and water saturation (α, ξ). The last data point indicated by the circle, at about $\phi = 0.55$, was best fit by the set of α = 1/160 and ξ = 0.6.

Figure 15 shows the estimated crack aspect ratio α and degree of water saturation ξ as a function of time. The aspect ratio changed from 1/400 to about 1/160 during the deformation as a result of water injection. Water saturation in the middle of the sample increased from 0 to 0.6.

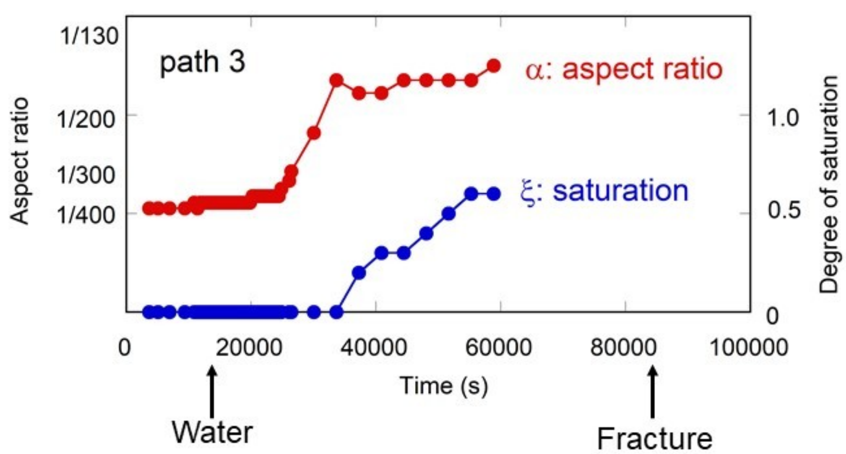

Figure 15

Figure 15. Changes in the aspect ratio (red) and water saturation (blue) at the midpoint of the sample as a function of time. The arrows labeled "Water" and "Fracture" mark the times when water injection started and when the rock sample fractured, respectively.

5. Conclusions

We demonstrated an in situ monitoring method for estimating crack shape and degree of water saturation from measured P- and S-wave velocities and porosity changes in the laboratory. We fractured an instrumented rock sample by injecting it with water under well-controlled differential stress and confining pressure conditions. We estimated the crack aspect ratio and the degree of water saturation by applying a cracked solid model to our experimental data on P- and S-wave velocities and crack density. We observed that (1) the aspect ratio α of dry cracks before water injection was 1/400, (2) during the water migration the aspect ratio changed from 1/400 to 1/160, and (3) the degree of water saturation ξ increased from 0 to 0.6. The monitoring methods described in this study may be useful in the estimation of microcracking at depth. Reliable monitoring methods for detecting crack characteristics and their time variation will aid in planning industrial and scientific applications including measurement of regional stress fields, induced seismicity, and sequestration of carbon dioxide and other waste.

Acknowledgments and Data Availability

T. Maruyama of the University of Tsukuba contributed to the experimental study. O. Nishizawa and X. Lei of the Geological Survey of Japan contributed to the data manipulation.

The data underlying this article are available in the article and in its online supplementary material.

References

Anderson, D. L., Minster, B., & Cole, D. (1974). The effect of oriented cracks on seismic velocities. *J. Geophys. Res.*, 79(26), 4011-4015, DOI: https://doi.org/10.1029/JB079i026p04011

Avseth, P., Mukerji, T., & Mavko, G. (2005). *Quantitative seismic interpretation, Applying rock physics tools to reduce interpretation risk*, UK: Cambridge Univ. Press.

Baines, S. J., & Worden, R. H. (Eds.) (2004). *Geological Storage of Carbon Dioxide*, Special Publications, 233, London: Geological Society.

Benson, P. M., Vinciguerra, S., Meredith, P. G., & Young R. P. (2008). Laboratory simulation of volcano seismicity, *Science*, 322, 249-252, DOI: 10.1126/science.1161927

Brace, W., Paulding, B., & Scholz, C. (1966). Dilatancy in the Fracture of Crystalline Rocks, *J. Geophys. Res.*, 71, 16, doi:10.1029/JZ071i016p03939

Budiansky, B., & O'Connell, R. J. (1976). Elastic moduli of a cracked solid, *International J. Solids Struct.*, 12, 81-97, http://dx.doi.org/10.1016/0020-7683(76)90044-5

Burlini, L., Di Toro, G., & Meredith, P. (2009). Seismic tremor in subduction zones: Rock physics evidence, *Geophys. Res. Lett.*, 36, L08305, doi:10.1029/2009GL037735

Caine, J. S., Evans, J. P., & Forster, C. B. (1996). Fault zone architecture and permeability structure, *Geology*, 24, 1025-1028, doi:10.1130/0091-7613 (1996) 024<1025:FZAAPS>2.3.CO;2

Crampin, S. (1978). Seismic wave propagation through a cracked solid: Polarization as a possible dilatancy diagnostic, *Geophys. J. Royal Astr. Soc.,* 53, 467-496, DOI: 10.1111/j.1365-246X.1978.tb03754.x

Crampin, S. (1984), Effective anisotropic elastic constants for wave propagation through cracked solids, *Geophys. J. Royal Astr. Soc.*, 76, 135-145, DOI: 10.1111/j.1365-246X.1984.tb05029.x

Ellsworth, W. L. (2013). Injection-Induced Earthquakes. *Science* 341, 1225942. DOI: 10.1126/science.1225942

Eyre, T. S., Eaton, D. W., Garagash, D. I., Zecevic, M., Venieri, M., Weir, R., & Lawton, D. C. (2019). The role of aseismic slip in hydraulic fracturing–induced seismicity. *Science Advances*, 5(8), eaav7172. DOI: 10.1126/sciadv.aav7172

Eyre, T. S., Zecevic, M., Salvage, R. O., & Eaton, D. W. (2020). A long-lived swarm of hydraulic fracturing-induced seismicity provides evidence for aseismic slip, *Bull. Seism. Soc. Am.,* 110, 2205–2215. doi: 10.1785/0120200107

Fehler, M. C. (1989), Stress control of seismicity patterns observed during hydraulic fracturing experiments at the Fenton Hill hot dry rock geothermal energy site, New Mexico, *Int. J. Rock Mech. Min. Sci. & Geomech. Abstr.*, 26, 211-219, http://dx.doi.org/ 10.1016/0148-9062(89)91971-2

Fossen, H. (2010), *Structural Geology*, UK: Cambridge Univ. Press.

Hangx, S. J. T., Spiers, C. J., & Peach, C. J. (2010). Mechanical behavior of anhydrite caprock and implications for CO2 sealing capacity, *J. Geophys. Res.*, 115, B07402, doi:10.1029/2009JB006954

Healy, J. H., Rubey, W. W., Griggs, D. T., & Raleigh, C. B. (1968). The Denver earthquakes, *Science*, 161, 1301-1310, doi:10.1126/ science.161.3848.1301

Hudson, J. A. (1981). Wave speeds and attenuation of elastic waves in material containing cracks, *Geophys. J. Royal Astr. Soc.*, 64, 133-150, DOI: 10.1111/j.1365-246X.1981.tb02662.x

Jost, M. L., Büßelberg, T., Jost, Ö., & Harjes, H.-P. (1998) Source parameters of injection-induced microearthquakes at 9 km depth at the KTB deep drilling site, Germany, *Bull. Seism. Soc. Am.*, 88, 815-832

Kranz, R. L., Satoh, T., Nishizawa, O., Kusunose, K., Takahashi, M., Masuda, K., & Hirata, A. (1990). Laboratory study of fluid pressure diffusion in rock using acoustic emissions, *J. Geophys. Res.*, 95(B13), 21,593–21,607, doi:10.1029/JB095iB13p21593

Lei, X., Masuda, K., Nishizawa, O., Jouniaux, L., Liu, L., Ma, W., Satoh, T., & Kusunose, K. (2004). Detailed analysis of acoustic emission activity during catastrophic fracture of faults in rock, *J. Struct. Geol.*, 26, 247–258, http://dx.doi.org/10.1016/S0191-8141(03)00095-6

Lei, X., Yu, G., Ma, S., Wen, X., & Wang, Q. (2008). Earthquakes induced by water injection at ~3 km depth within the Rongchang gas field, Chongqing, China, *J. Geophys. Res.*, 113, B10310, doi:10.1029/2008JB005604

Lockner, D., & Byerlee, J. D. (1977). Hydrofracture in Weber sandstone at high confining pressure and differential stress, *J. Geophys. Res.*, 82(14), 2018–2026, doi:10.1029/JB082i014p02018

Lockner, D. A., Byerlee, J. D., Kuksenko, V., Ponomarev, A., & Sidorin, A. (1991). Quasi-static fault growth and shear fracture energy in granite, *Nature*, 350, 39-42, doi:10.1038/350039a0

Masuda, K., Nishizawa, O., Kusunose, K., Satoh, T., Takahashi, M., & Kranz, R. L. (1990). Positive feedback fracture process induced by nonuniform high-pressure water flow in dilatant granite, *J. Geophys. Res.*, 95(B13), 21,583–21,592, doi:10.1029/JB095iB13p21583

Masuda, K., Nishizawa, O., Kusunose, K., & Satoh, T. (1993). Laboratory study of effects of in situ stress state and strength on fluid-induced seismicity, *Int. J. Rock Mech. Min. Sci. & Geomech. Abstr.*, 30, 1-10, http://dx.doi.org/10.1016/0148-9062(93)90171-9

Masuda, K., Arai, T., Fujimoto, K., Takahashi, M., & Shigematsu, N. (2012). Effect of water on weakening preceding rupture of laboratory-scale faults: Implications for long-term weakening of crustal faults, *Geophys. Res. Lett.*, 39, L01307, doi:10.1029/2011GL050493

Masuda, K. (2013). Source duration of stress and water-pressure induced seismicity derived from experimental analysis of P wave pulse width in granite. *Geophys. Res. Lett.*, 40, 3567-3571, DOI: 10.1002/grl.50691

Masuda, K., Satoh, T., & Nishizawa, O. (2013). Ultrasonic transmission and acoustic emission monitoring of injection-induced fracture processes in rock samples, *Proceedings of the 47th US Rock Mechanics/Geomechanics Symposium* 23-26 June 2013, San Francisco, California, USA, ARMA13-295

Mavko, G., Mukerji, T., & Dvorkin, J. (2009). *The rock physics handbook*, 2nd ed., UK: Cambridge Univ. Press.

Meglis, I. L., Greenfield, R. J., Engelder, T., & Graham, E. K. (1996). Pressure dependence of velocity and attenuation and its relationship to crack closure in crystalline rocks, *J. Geophys. Res.*, 101(B8), 17,523–17,533, doi:10.1029/96JB00107

Moore, D. E., & Lockner, D. A. (1995). The role of microcracking in shear-fracture propagation in granite, *J. Struct. Geol.*, 17, 95–114, http://dx.doi.org/10.1016/0191-8141(94)E0018-T

Nishizawa, O., & Masuda, K. (1991). Characterization of microcracks estimated from

P-wave velocity change caused by high-pressure water flow in dilatant granite, Geophysical Exploration (Butsuri-tansa), 44, 255-265 (in Japanese with English abstract)

O'Connell, R. J., & Budiansky, B. (1974). Seismic velocities in dry and saturated cracked solids, *J. Geophys. Res.*, 79(35), 5412–5426, doi:10.1029/JB079i035p05412

Ohtake, M. (1987). Temporal change of Q_p^{-1} in focal area of 1984 western Nagano, Japan, earthquake as derived from pulse width analysis, *J. Geophys. Res.*, 92(B6), 4846–4852, doi:10.1029/JB092iB06p04846

Paterson, M. S., & Wong, T-F. (2005). *Experimental rock deformation – The brittle field*, 2nd ed., NY, Springer.

Prioul, R., Cornet, F. H., Dorbath, C., Dorbath, L., Ogena, M., & Ramos, E. (2000). An induced seismicity experiment across a creeping segment of the Philippine Fault, *J. Geophys. Res.*, 105(B6), 13,595–13,612, doi:10.1029/2000JB900052

Raleigh, C. B., Healy, J. H., & Bredehoeft, J. D. (1976). An experiment in earthquake control at Rangely, Colorado, *Science*, 191, 1230–1237, doi:10.1126/science.191.4233.1230, doi:10.1126/science.191.4233.1230

Rutqvist, J., Birkholzer, J. T., & Tsang, C.-F. (2008). Coupled reservoir–geomechanical analysis of the potential for tensile and shear failure associated with CO2 injection in multilayered reservoir–caprock systems, *Int. J. Rock Mech. Min. Sci.*, 45, 132–143, http://dx.doi.org/10.1016/j.ijrmms.2007.04.006

Scholz, C. H. (1968), Experimental study of the fracturing process in brittle rock, *J. Geophys. Res.*, 73(4), 1447–1454, doi:10.1029/JB073i004p01447

Scholz, C. H., (2002), *The mechanics of earthquakes and faulting*, 2nd ed., UK: Cambridge

Univ. Press.

Schön, J. H., (2011), *Physical properties of rocks: A Workbook, Handbook of Petroleum Exploration and Production, 8*, GB, Elsevier.

Schubnel, A., Nishizawa, O., Masuda, K., Lei, X., Xue, Z., & Guégen, Y. (2003). Velocity measurements and crack density determination during wet triaxial experiments on Oshima and Toki granites, *Pure appl. Geophys.*, 160, 869-887, doi:10.1007/PL00012570

Schultz, R., Wang, R., Gu, Y. J., Haug, K. & Atkinson, G. (2017). A seismological overview of the induced earthquakes in the Duvernay play near Fox Creek, Alberta, *J. Geophys. Res.: Solid Earth*, 122, 492–505. doi:10.1002/2016JB013570

Schultz, R., Atkinson, G., Eaton, D. W., Gu, Y. J., & Kao, H. (2018). Hydraulic fracturing volume is associated with induced earthquake productivity in the Duvernay play. *Science* 359 (6373), 304-308. DOI: 10.1126/science.aao0159

Schultz, R., Skoumal, R. J., Brudzinski, M. R., Eaton, D., Baptie, B., & Ellsworth, W. (2020). Hydraulic fracturing‐induced seismicity. *Rev. Geophys.*, 58, e2019RG000695. https://doi.org/10.1029/2019RG000695

Soga, N., Mizutani, H., Spetzler, H., & Martin III, R. J. (1978). The effect of dilatancy on velocity anisotropy in Westerly granite, *J. Geophys. Res.*, 83(B9), 4451–4458, doi:10.1029/JB083iB09p04451

Stanchits, S., Mayr, S., Shapiro, S., & Dresen, G. (2011). Fracturing of porous rock induced by fluid injection, *Tectonophysics*, 503, 129-145, http://dx.doi.org/10.1016/j.tecto.2010.09.022

Wang, Z., Lei, X., Ma, S., Wang, X., & Wan, Y. (2020). Induced earthquakes before and after cessation of long−term injections in Rongchang gas field. *Geophys. Res. Lett.*, 47, e2020GL089569. https://doi.org/10.1029/2020GL089569

Wong, T.-F. (1982). Micromechanics of faulting in Westerly granite, *Int. J. Rock Mech. Min. Sci. & Geomech. Abstr.*, 19, 49–64, http://dx.doi.org/10.1016/0148-9062(82)91631-X

Zoback, M. D., & Harjes, H.-P. (1997). Injection-induced earthquakes and crustal stress at 9 km depth at the KTB deep drilling site, Germany, *J. Geophys. Res.*, 102(B8), 18,477–18,491, doi:10.1029/96JB02814

Appendix A: Elastic constants of rock material for the case of transversely isotropic symmetry along the x-3 axis (z-axis) with randomly distributed vertical cracks

Here we describe the method of calculation of elastic constants for the case in which plane normals of cracks are randomly distributed in directions perpendicular to the x-3 axis (z-axis). We also show that the ratio of the elastic constant of rock material that includes cracks to that of the matrix or the square of velocity ratio is expressed as $(V/V_0)^2 = 1 - p_i\,\varepsilon$, where V and V_0 are the elastic-wave velocities with and without cracks, respectively, and ε is the crack density parameter defined by

$$\varepsilon = \frac{3\varnothing}{4\pi\alpha}, \qquad \text{(A1)}$$

where ∅ is the porosity and α = c/a is the aspect ratio of the crack ($a = b \gg c$). In addition, we derive the coefficients p_i.

The focus of this study is on a transversely isotropic medium with the x-3 axis (z-axis) as the axis of symmetry and with a vertical crack distribution in which the plane normals of the cracks are randomly distributed in horizontal directions (directions parallel to the x-1,2 plane, x-y plane). The right-handed rectangular coordinate system is used in this study (Figure S1a).

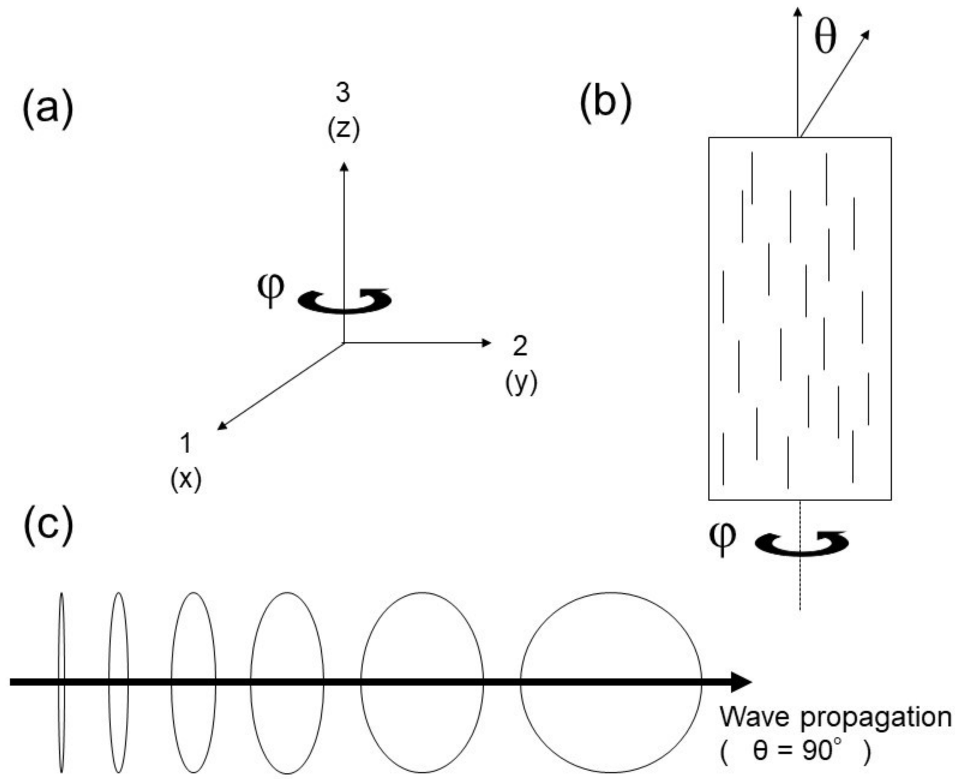

Figure S1

Figure S1. The basic assumptions in this study: (a) the coordinate system, (b) vertical cross section of transversely isotropic rock with vertical cracks, and (c) side view of the direction of wave propagation and crack distribution.

First, based on the method of Hudson (1981), we calculated C_{ij} for a material that includes vertical cracks that are plane normal along the x-1 axis (x-axis) (Figure S1b). Next, we took the rotational average of C_{ij} around the x-3 axis (z-axis), resulting in $\widehat{C}_{ij}$, which were shown to be transversely isotropic with the x-3 axis (z-axis) by using a method similar to that of Nishizawa and Masuda (1991).

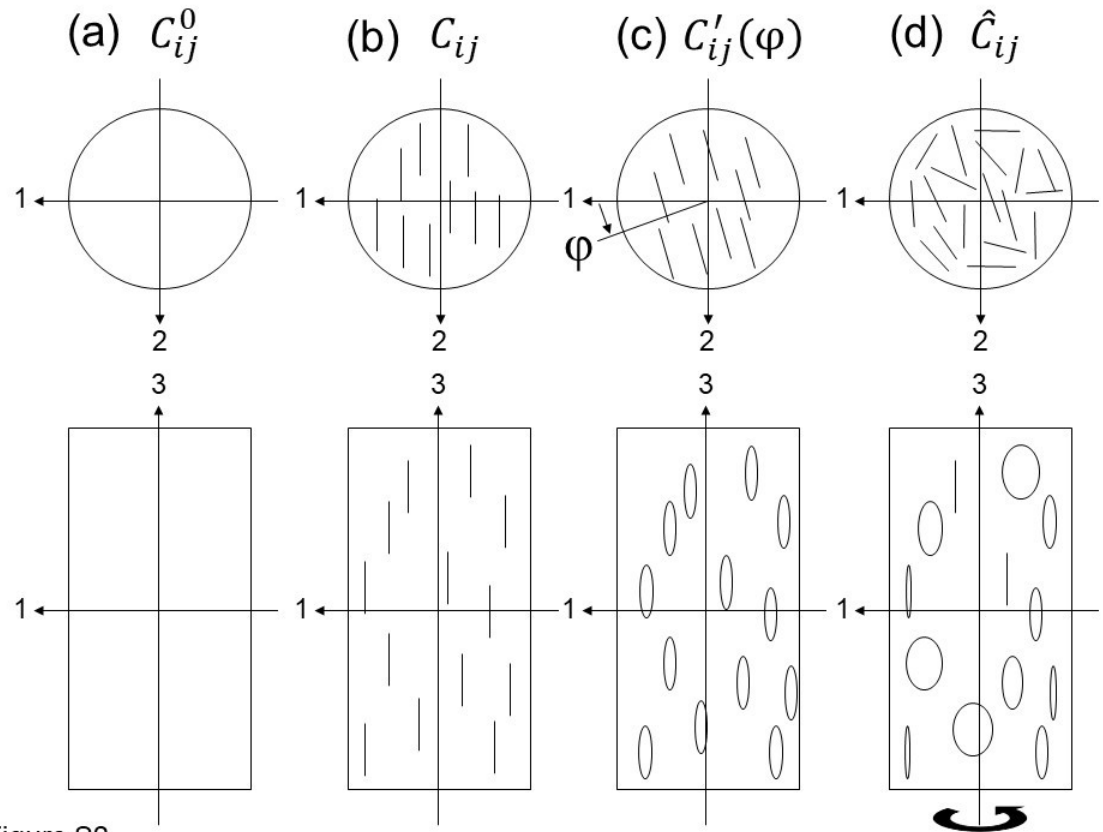

Figure S2

Figure S2. Procedure for calculating the elastic constants in the transversely isotropic rock with vertical cracks: (a) C_{ij}^{0} elastic constants of the rock matrix; (b) C_{ij} elastic constants for the rock material with vertical cracks for which the plane-normal direction is along the x-1 axis (x-axis); (c) $C'_{ij}(\varphi)$ elastic constants for rock material with vertical cracks for which the angle between the plane-normal direction and the x-1 axis (x-axis) is φ; and (d) $\widehat{C}_{ij}$ elastic constants for rock material with transversely isotropic symmetry along the x-3 axis (z-axis) with vertical cracks with random values of φ.

1. C_{ij}^{0} elastic constants of the isotropic rock matrix (Figure S2a)

In this study, we use abbreviated 2-index Voigt notation to express elastic constants such as C_{ij} instead of 4-index notation for the fourth-rank tensor c_{ijkl}. We assume that the matrix of rock without cracks or inclusions is isotropic with two independent constants:

$$C_{ij}^0 = \begin{pmatrix} C_{11}^0 & C_{12}^0 & C_{12}^0 & 0 & 0 & 0 \\ C_{12}^0 & C_{11}^0 & C_{12}^0 & 0 & 0 & 0 \\ C_{12}^0 & C_{12}^0 & C_{11}^0 & 0 & 0 & 0 \\ 0 & 0 & 0 & C_{44}^0 & 0 & 0 \\ 0 & 0 & 0 & 0 & C_{44}^0 & 0 \\ 0 & 0 & 0 & 0 & 0 & C_{44}^0 \end{pmatrix} = \begin{pmatrix} \lambda+2\mu & \lambda & \lambda & 0 & 0 & 0 \\ \lambda & \lambda+2\mu & \lambda & 0 & 0 & 0 \\ \lambda & \lambda & \lambda+2\mu & 0 & 0 & 0 \\ 0 & 0 & 0 & \mu & 0 & 0 \\ 0 & 0 & 0 & 0 & \mu & 0 \\ 0 & 0 & 0 & 0 & 0 & \mu \end{pmatrix} \quad \text{(A2)}$$

$$C_{12}^0 = C_{11}^0 - 2C_{44}^0 \quad \text{(A3)}$$

The relationships between the elements C_{ij}^0 and Lame's parameters λ and μ of isotropic linear elasticity are

$$C_{11}^0 = \lambda + 2\mu, C_{12}^0 = \lambda, C_{44}^0 = \mu. \quad \text{(A4)}$$

2. C_{ij} elastic constants for rock material with cracks that are plane normal along the x-1 axis (x-axis) (Figure S2b)

Hudson (1981) modeled fractured rock as an elastic solid with thin, penny-shaped ellipsoidal cracks or inclusions. The effective moduli C_{ij} are given as

$$C_{ij} = C^0_{ij} + C^1_{ij}, \quad \text{(A5)}$$

where C^0_{ij} are the isotropic background moduli and C^1_{ij} are the first-order corrections. For the case in which the vertical cracks have crack normals along the x-1 axis (x-axis), the axis of symmetry of the material lies along the x-1 axis (x-axis), which has hexagonal symmetry with five independent constants as

$$C^1_{ij} = \begin{pmatrix} C^1_{11} & C^1_{12} & C^1_{12} & 0 & 0 & 0 \\ C^1_{12} & C^1_{22} & C^1_{23} & 0 & 0 & 0 \\ C^1_{12} & C^1_{23} & C^1_{22} & 0 & 0 & 0 \\ 0 & 0 & 0 & C^1_{44} & 0 & 0 \\ 0 & 0 & 0 & 0 & C^1_{55} & 0 \\ 0 & 0 & 0 & 0 & 0 & C^1_{55} \end{pmatrix}, C^1_{44} = \frac{1}{2}\left(C^1_{22} - C^1_{23}\right). \quad \text{(A6)}$$

The following correction terms are given by Schön (2011, Table 6.15) for the case in which the crack normals are aligned along the x-1 axis (x-axis), including the vertical cracks:

$$C^1_{11} = \frac{-(\lambda + 2\mu)^2}{\mu} \varepsilon U_3 \quad \text{(A7)}$$

$$C^1_{13} = \frac{-\lambda(\lambda + 2\mu)^2}{\mu} \varepsilon U_3 \quad \text{(A8)}$$

$$C^1_{33} = \frac{-\lambda^2}{\mu} \varepsilon U_3 \quad \text{(A9)}$$

$$C_{44}^{1}=0 \quad \text{(A10)}$$

$$C_{66}^{1}=-\mu\varepsilon U_1 \quad \text{(A11)}$$

in which the correction terms C_{ij}^{1} are negative; thus, the elastic properties decrease with fracturing. U_1 and U_3 depend on the crack conditions (Mavko et al., 2009; Schon 2011). For dry cracks,

$$U_1=\frac{16(\lambda+2\mu)}{3(3\lambda+4\mu)};U_3=\frac{4(\lambda+2\mu)}{3(\lambda+\mu)}. \quad \text{(A12)}$$

For wet cracks, Hudson’s expressions for infinitely thin fluid-filled cracks are

$$U_1=\frac{16(\lambda+2\mu)}{3(3\lambda+4\mu)};U_3=0. \quad \text{(A13)}$$

Therefore, for the dry case, C_{ij} are

$$C_{11}=C_{11}^{0}+C_{11}^{1}=(\lambda+2\mu)(1-6\varepsilon) \quad \text{(A14)}$$

$$C_{13}=C_{13}^{0}+C_{13}^{1}=\lambda(1-6\varepsilon) \quad \text{(A15)}$$

$$C_{33}=C_{33}^{0}+C_{33}^{1}=(\lambda+2\mu)\left(1-\frac{2}{3}\varepsilon\right) \qquad \text{(A16)}$$

$$C_{44}=C_{44}^{0}+C_{44}^{1}=\mu \qquad \text{(A17)}$$

$$C_{66}=C_{66}^{0}+C_{66}^{1}=\mu\left(1-\frac{16}{7}\varepsilon\right). \qquad \text{(A18)}$$

For the wet case,

$$C_{11}=C_{11}^{0}+C_{11}^{1}=\lambda+2\mu \qquad \text{(A19)}$$

$$C_{13}=C_{13}^{0}+C_{13}^{1}=\lambda \qquad \text{(A20)}$$

$$C_{33}=C_{33}^{0}+C_{33}^{1}=\lambda+2\mu \qquad \text{(A21)}$$

$$C_{44}=C_{44}^{0}+C_{44}^{1}=\mu \qquad \text{(A22)}$$

$$C_{66}=C_{66}^{0}+C_{66}^{1}=\mu\left(1-\frac{16}{7}\varepsilon\right). \qquad \text{(A23)}$$

C_{ij} has hexagonal symmetry with the x-1 axis (x-axis) expressed with five independent moduli.

3. $C'_{ij}(\varphi)$ elastic constants for rock material with vertical cracks that have an angle φ between the plane-normal direction and the x-1 axis (x-axis) (Figure S2c)

When we rotate C_{ij} around the x-3 axis (z-axis) by an angle of φ from the x-1 axis (x axis), C_{ij} is a function of φ, as expressed by $C'_{ij}(\varphi)$.

Regarding coordinate transformations, the elastic compliances c_{ijkl} are, in general, fourth-rank tensors and hence transform according to

$$c'_{ijkl} = \beta_{ip}\beta_{jq}\beta_{kr}\beta_{ls}c_{pqrs}, \qquad \text{(A24)}$$

where c'_{ijkl} and c_{pqrs} are the elastic compliances after and before the coordinate transformation, respectively. For rotation around the x-3 axis (z-axis), β_{ij} is the following matrix element

$$\begin{pmatrix} \cos\varphi & \sin\varphi & 0 \\ -\sin\varphi & \cos\varphi & 0 \\ 0 & 0 & 1 \end{pmatrix}. \qquad \text{(A25)}$$

In this study, we use the abbreviated 2-index Voigt notation C_{ij} instead of c'_{ijkl} and c_{ijkl}. Although an elastic constant looks like a second-rank tensor (C_{ij}) with this notation, it is indeed a fourth-rank tensor; when one performs a coordinate transformation, one must go back to the full notation and follow the transformation rules for a fourth-rank tensor. The usual tensor transformation law is no longer valid. However, the change of coordinates for $C_{ij}$is more efficiently performed with the 6 × 6 Bond Transformation Matrices, **M** (Mavko et al., 2009). The advantage of the Bond method for transforming compliances is that it can be applied directly to the elastic constants given in 2-index notation, as expressed as follows:

$$[C'] = [M][C][M]^T \qquad \text{(A26)}$$

M

$$¿\begin{bmatrix} \beta_{11}^2 & \beta_{12}^2 & \beta_{13}^2 & 2\beta_{12}\beta_{13} & 2\beta_{13}\beta_{11} & 2\beta_{11}\beta_{12} \\ \beta_{21}^2 & \beta_{22}^2 & \beta_{23}^2 & 2\beta_{22}\beta_{23} & 2\beta_{23}\beta_{21} & 2\beta_{21}\beta_{22} \\ \beta_{31}^2 & \beta_{32}^2 & \beta_{33}^2 & 2\beta_{32}\beta_{33} & 2\beta_{33}\beta_{31} & 2\beta_{31}\beta_{32} \\ \beta_{21}\beta_{31} & \beta_{22}\beta_{32} & \beta_{23}\beta_{33} & \beta_{22}\beta_{33}+\beta_{23}\beta_{32} & \beta_{21}\beta_{33}+\beta_{23}\beta_{31} & \beta_{22}\beta_{31}+\beta_{21}\beta_{32} \\ \beta_{31}\beta_{11} & \beta_{32}\beta_{12} & \beta_{33}\beta_{13} & \beta_{12}\beta_{33}+\beta_{13}\beta_{32} & \beta_{11}\beta_{33}+\beta_{13}\beta_{31} & \beta_{11}\beta_{32}+\beta_{12}\beta_{31} \\ \beta_{11}\beta_{21} & \beta_{12}\beta_{22} & \beta_{13}\beta_{23} & \beta_{22}\beta_{13}+\beta_{12}\beta_{23} & \beta_{11}\beta_{23}+\beta_{13}\beta_{21} & \beta_{22}\beta_{11}+\beta_{12}\beta_{21} \end{bmatrix}.$$

(A27)

Then, we obtain $C'_{ij}(\varphi)$ as

$$C'_{11}(\varphi) = \cos^4\varphi\, C_{11} + 2\sin^2\varphi\cos^2\varphi\, C_{12} + \sin^4\varphi\, C_{22} + 4\sin^2\varphi\cos^2\varphi\, C_{55} \qquad \text{(A28)}$$

$$C'_{22}(\varphi) = \sin^4\varphi\, C_{11} + 2\sin^2\varphi\cos^2\varphi\, C_{12} + \cos^4\varphi\, C_{22} + 4\sin^2\varphi\cos^2\varphi\, C_{55} \qquad \text{(A29)}$$

$$C'_{12}(\varphi) = C'_{21}(\varphi) = \sin^2\varphi\cos^2\varphi\, C_{11} + \left(\sin^4\varphi + \cos^4\varphi\right) C_{12} + \sin^2\varphi\sin^2\varphi\, C_{22} - 4\sin^2\varphi\cos^2\varphi\, C_{55}$$

(A30)

$$C'_{13}(\varphi) = C'_{31}(\varphi) = \cos^2\varphi\, C_{12} + \sin^2\varphi\, C_{23} \qquad \text{(A31)}$$

$$C'_{23}(\varphi)=C'_{32}(\varphi)=\sin^2\varphi\, C_{12}+\cos^2\varphi\, C_{23} \qquad \text{(A32)}$$

$$C'_{33}(\varphi)=C_{22} \qquad \text{(A33)}$$

$$C'_{44}(\varphi)=\cos^2\varphi\, C_{44}+\sin^2\varphi\, C_{55} \qquad \text{(A34)}$$

$$C'_{55}(\varphi)=\sin^2\varphi\, C_{44}+\cos^2\varphi\, C_{55} \qquad \text{(A35)}$$

$$C'_{66}(\varphi)=\sin^2\varphi\cos^2\varphi\, C_{11}-2\sin^2\varphi\cos^2\varphi\, C_{12}+\sin^2\varphi\cos^2\varphi\, C_{22}+(\cos^2\varphi-\sin^2\varphi)^2 C_{55}. \qquad \text{(A36)}$$

The following non-zero elements are zero in the next step 4, taking the rotational average:

$$C'_{16}(\varphi), C'_{61}(\varphi), C'_{26}(\varphi), C'_{62}(\varphi), C'_{36}(\varphi), C'_{63}(\varphi), C'_{45}(\varphi), C'_{54}(\varphi).$$

4. $\widehat{C}_{ij}$ elastic constants for rock material with transversely isotropic symmetry along the x-3 axis (z-axis) and a vertical crack distribution (Figure S2d)

We took the rotational average of C_{ij} around the x-3 axis (z-axis) to obtain $\widehat{C}_{ij}$that showed transversely isotropic symmetry along the x-3 axis (z-axis) in the case of a random vertical crack distribution as follows:

$$\widehat{C}_{ij}=\frac{1}{2\pi}\int_{0}^{2\pi} C'_{ij}(\varphi)\,d\varphi, \qquad \text{(A37)}$$

which uses

$$\frac{1}{2\pi}\int_{0}^{2\pi}\sin^4\varphi\,d\varphi=\frac{3}{8},\frac{1}{2\pi}\int_{0}^{2\pi}\cos^4\varphi\,d\varphi=\frac{3}{8},\frac{1}{2\pi}\int_{0}^{2\pi}\sin^2\varphi\cos^2\varphi\,d\varphi=\frac{1}{8},$$

(A38)

$$\frac{1}{2\pi}\int_{0}^{2\pi}\sin^2\varphi\,d\varphi=\frac{1}{2},\frac{1}{2\pi}\int_{0}^{2\pi}\cos^2\varphi\,d\varphi=\frac{1}{2}. \qquad \text{(A39)}$$

$\widehat{C}_{ij}$ shows hexagonal symmetry or transversely isotropic symmetry with the x-3 axis (z-axis) in which there are five independent constants:

$$\widehat{C}_{11}=\frac{1}{2\pi}\int_{0}^{2\pi} C'_{11}(\varphi)\,d\varphi=\frac{3}{8}C_{11}+\frac{1}{4}C_{12}+\frac{3}{8}C_{22}+\frac{1}{2}C_{55} \quad \text{(A40)}$$

$$\widehat{C}_{12}=\frac{1}{2\pi}\int_{0}^{2\pi} C'_{12}(\varphi)\,d\varphi=\frac{1}{8}C_{11}+\frac{3}{4}C_{12}+\frac{1}{8}C_{22}-\frac{1}{2}C_{55} \quad \text{(A41)}$$

$$\widehat{C}_{13}=\frac{1}{2\pi}\int_{0}^{2\pi} C'_{13}(\varphi)\,d\varphi=\frac{1}{2}C_{12}+\frac{1}{2}C_{23} \quad \text{(A42)}$$

$$\widehat{C}_{33}=C_{22} \quad \text{(A43)}$$

$$\widehat{C}_{44}=\frac{1}{2\pi}\int_{0}^{2\pi} C'_{44}(\varphi)\,d\varphi=\frac{1}{2}C_{44}+\frac{1}{2}C_{55} \quad \text{(A44)}$$

$$\widehat{C}_{66}=\frac{1}{2\pi}\int_{0}^{2\pi} C'_{66}(\varphi)\,d\varphi=\frac{1}{8}C_{11}-\frac{1}{4}C_{12}+\frac{1}{8}C_{22}+\frac{1}{2}C_{55}=\frac{1}{2}\left(\widehat{C}_{11}-\widehat{C}_{12}\right). \quad \text{(A45)}$$

5. Wave velocities which propagate in the horizontal directions

In the material with transversely isotropic symmetry, there are three modes of wave propagation, and their velocities are dependent on the angle θ between the axis of symmetry (in this case, x-3 axis or z-axis) and the direction of the wave vector:

$$V_P=\sqrt{\frac{\widehat{C}_{11}\sin^2\theta+\widehat{C}_{33}\cos^2\theta+\widehat{C}_{44}+A}{2\rho}} \quad \text{(A46)}$$

$$V_{SV}=\sqrt{\frac{\widehat{C}_{11}\sin^2\theta+\widehat{C}_{33}\cos^2\theta+\widehat{C}_{44}-A}{2\rho}} \quad \text{(A47)}$$

$$V_{SH}=\sqrt{\frac{\widehat{C}_{66}\sin^2\theta+\widehat{C}_{44}\cos^2\theta}{2\rho}}, \quad \text{(A48)}$$

where $A=\sqrt{\left[\left(\widehat{C}_{11}-\widehat{C}_{44}\right)\sin^2\theta+\left(\widehat{C}_{33}-\widehat{C}_{44}\right)\cos^2\theta\right]^2+\left(\widehat{C}_{13}+\widehat{C}_{44}\right)^2\sin^2 2\theta}$. (A49)

For θ = 90°, the relationship simplifies to $A=\hat{C}_{33}-\hat{C}_{44}$ and the wave velocity vectors that propagate perpendicular to the x-3 axis in horizontal directions (Figure S1c) are

$$V_P=\sqrt{\frac{\hat{C}_{11}}{\rho}},V_{SV}=\sqrt{\frac{\hat{C}_{44}}{\rho}},V_{SH}=\sqrt{\frac{\hat{C}_{66}}{\rho}}, \quad \text{(A50)}$$

where V_P, V_{SV}, and V_{SH} are the longitudinal-wave velocity, shear-wave velocity with vertical polarization, and shear-wave velocity with horizontal polarization, respectively.

We consider low-porosity aggregate and flat cracks, and have ignored the effect of porosity on the density of the composite (Anderson et al., 1974).

For the dry case, using $\lambda=\mu$,

$$V_P^2=\frac{\hat{C}_{11}}{\rho}=\frac{\lambda+2\mu}{\rho}\left(1-\frac{71}{21}\varepsilon\right)=V_{P0}^2\left(1-\frac{71}{21}\varepsilon\right) \quad \text{(A51)}$$

$$V_{SV}^2=\frac{\hat{C}_{44}}{\rho}=\frac{\mu}{\rho}\left(1-\frac{8}{7}\varepsilon\right)=V_{SV0}^2\left(1-\frac{8}{7}\varepsilon\right) \quad \text{(A52)}$$

$$V_{SH}^2=\frac{\hat{C}_{66}}{\rho}=\frac{\mu}{\rho}\left(1-\frac{15}{7}\varepsilon\right)=V_{SH0}^2\left(1-\frac{15}{7}\varepsilon\right), \quad \text{(A53)}$$

where V with a subscript 0 are the velocities without cracks.

For the wet case,

$$V_P^2 = \frac{\widehat{C}_{11}}{\rho} = \frac{\lambda + 2\mu}{\rho}\left(1 - \frac{8}{21}\varepsilon\right) = V_{P0}^2\left(1 - \frac{8}{21}\varepsilon\right) \quad \text{(A54)}$$

$$V_{SV}^2 = \frac{\widehat{C}_{44}}{\rho} = \frac{\mu}{\rho}\left(1 - \frac{8}{7}\varepsilon\right) = V_{SV0}^2\left(1 - \frac{8}{7}\varepsilon\right) \quad \text{(A55)}$$

$$V_{SH}^2 = \frac{\widehat{C}_{66}}{\rho} = \frac{\mu}{\rho}\left(1 - \frac{8}{7}\varepsilon\right) = V_{SH0}^2\left(1 - \frac{8}{7}\varepsilon\right). \quad \text{(A56)}$$

The effect of cracks on velocity, in terms of the ratio of velocities with and without cracks, is proportional to the crack density parameter ε at small values of ε:

$$\left(\frac{V}{V_0}\right)^2 = 1 - p_i\varepsilon. \quad \text{(A57)}$$

Supporting Information

Data1. Experimental conditions of applied stress and water pressure (Figure 1)

Data2. Number of AE events detected every 2000s (Figure 1)

Data3. P-wave velocity (Figure 4)

Data4. Sv-wave velocity (Figure 5)

Data5. Sh-wave velocity (Figure 5)

Data6. Strain data (Figure 7)

Data7. AE location data (Figure 8)